JGP Journal of General Physiology

RESEARCH ARTICLE

Dynamic rearrangement of the intrinsic ligand regulates KCNH potassium channels

Gucan Dai, Zachary M. James, and William N. Zagotta

KCNH voltage-gated potassium channels (EAG, ERG, and ELK) play significant roles in neuronal and cardiac excitability. They contain cyclic nucleotide-binding homology domains (CNBHDs) but are not directly regulated by cyclic nucleotides. Instead, the CNBHD ligand-binding cavity is occupied by an intrinsic ligand, which resides at the intersubunit interface between the N-terminal eag domain and the C-terminal CNBHD. We show that, in *Danio rerio* ELK channels, this intrinsic ligand is critical for voltage-dependent potentiation (VDP), a process in which channel opening is stabilized by prior depolarization. We demonstrate that an exogenous peptide corresponding to the intrinsic ligand can bind to and regulate zebrafish ELK channels. This exogenous intrinsic ligand inhibits the channels before VDP and potentiates the channels after VDP. Furthermore, using transition metal ion fluorescence resonance energy transfer and a fluorescent noncanonical amino acid L-Anap, we show that there is a rearrangement of the intrinsic ligand relative to the CNBHD during VDP. We propose that the intrinsic ligand switches from antagonist to agonist as a result of a rearrangement of the eag domain–CNBHD interaction during VDP.

Introduction

Voltage-gated potassium (Kv) channels set the resting membrane potential, shorten the duration of action potentials, and dampen the excitatory inputs on neurons (Hille, 2001). First identified in *Drosophila melanogaster* as ether-à-go-go (EAG) potassium channels (Warmke et al., 1991), the KCNH subfamily of Kv channels consists of EAG, EAG-related gene (ERG), and EAG-like (ELK) subtypes and helps control the rhythmic heartbeat, hippocampal excitability, and cancer pathophysiology (Warmke and Ganetzky, 1994; Trudeau et al., 1995; Zhang et al., 2010; Pardo and Stühmer, 2014).

KCNH channels have a similar architecture but distinct functional properties compared with cyclic nucleotide-gated (CNG) and hyperpolarization-activated cyclic nucleotide-gated (HCN) channels (Whicher and MacKinnon, 2016; Wang and MacKinnon, 2017). They contain four subunits, each with six transmembrane segments divided into a voltage-sensor domain (S1–S4) and a pore domain (S5–S6). The intracellular parts of each subunit include an N-terminal eag domain and a C-terminal cyclic nucleotide-binding homology domain (CNBHD; Guy et al., 1991; Warmke and Ganetzky, 1994; Ganetzky et al., 1999; Whicher and MacKinnon, 2016; Lee and MacKinnon, 2017; Li et al., 2017; Wang and MacKinnon, 2017). However, KCNH channels are not directly activated by cyclic nucleotides like cAMP and cGMP (Robertson et al., 1996; Brelidze et al., 2009). Instead, an intrinsic ligand, which comprises three residues following the C helix of the CNB HD, occupies the ligand-binding pocket analogous to where cyclic nucleotides bind CNG and HCN channels (Fig. 1 A; Brelidze et al., 2012; Marques-Carvalho et al., 2012; Ng et al., 2013). In addition, the intrinsic ligand resides at the intersubunit interface between the CNBHD and the eag domain, which were shown to interact in both the EAG1 and human ERG1 (hERG1) structures (Haitin et al., 2013; Whicher and MacKinnon, 2016; Wang and MacKinnon, 2017). The eag domain comprises a Per-Arnt-Sim (PAS) domain and a short PAS cap (Fig. 1 A). This eag domain–CNBHD interaction has been shown to be critical for the activation, deactivation, and inactivation of KCNH channels (Terlau et al., 1997; Gustina and Trudeau, 2009; Gianulis et al., 2013; Haitin et al., 2013; Whicher and MacKinnon, 2016; Dai and Zagotta, 2017; Wang and MacKinnon, 2017). Previous experiments have shown that mutations and deletions of the intrinsic ligand affect the voltage-dependent gating of KCNH channels, although the effects vary depending on the channel subtype and particular mutation (Marques-Carvalho et al., 2012; Brelidze et al., 2013; Zhao et al., 2017). Furthermore, a long QT syndrome–related mutation in the intrinsic ligand of hERG channels, which causes cardiac arrhythmia, prevents functional expression of the channel (Splawski et al., 2000; Brelidze et al., 2013). Although the mechanisms for the cyclic nucleotide binding and activation of related CNG and HCN

Department of Physiology and Biophysics, University of Washington, Seattle, WA.

Correspondence to William N. Zagotta: zagotta@uw.edu.

channels have been well studied (Fesenko et al., 1985; Varnum et al., 1995; Craven and Zagotta, 2006), much is still unknown about how the intrinsic ligand and conformational changes of the CNB HD modulate the gating of KCNH channels.

Recently, we characterized a phenomenon in the zebrafish ELK (zELK) channel called voltage-dependent potentiation (VDP), where depolarizing voltages slowly transition the channel to a mode where opening is more favorable (Dai and Zagotta, 2017). This gating behavior, also shared by human ELK and hERG channels, manifests as a slow phase of the current increase with depolarizing voltage steps, a shift in the voltage dependence of activation to more hyperpolarized potentials, and slowing of deactivation after depolarizing prepulses (Tan et al., 2012; Goodchild et al., 2015; Li et al., 2015; Dai and Zagotta, 2017). VDP, previously called mode shift, prepulse facilitation, and hysteresis (Bean, 1989; Männikkö et al., 2005; Elinder et al., 2006), is suggested to be a specialization that reduces high-frequency firings of cardiac myocytes and neurons (Zhang et al., 2010). Mechanistically, VDP requires the direct interaction of the N-terminal eag domain and the C-terminal CNBHD (Gustina and Trudeau, 2009; Gianulis et al., 2013; Haitin et al., 2013; Whicher and MacKinnon, 2016; Dai and Zagotta, 2017; Wang and MacKinnon, 2017). Disrupting this interaction significantly attenuated VDP (Goodchild et al., 2015; Li et al., 2015; Dai and Zagotta, 2017). In addition, a slow rearrangement of the eag domain–CNBHD interaction accompanies the VDP of zELK channels, suggesting that VDP arises from a conformational change of intracellular domains coupled to voltage-dependent opening of the channel (Dai and Zagotta, 2017).

In this work, we studied the contribution of the intrinsic ligand to the gating of zELK channels using electrophysiological and fluorescence approaches. We found that a peptide corresponding to the intrinsic ligand could bind to the CNBHD and regulate channel gating. We then used two methods for simultaneously measuring structural rearrangements in the channel and ionic current: (1) voltage-clamp fluorometry (VCF) using a fluorescent noncanonical amino acid L-Anap (Kalstrup and Blunck, 2013; Sakata et al., 2016) and (2) patch-clamp fluorometry (PCF; Zheng and Zagotta, 2003) combined with transition metal ion fluorescence resonance energy transfer (tmFRET; Taraska et al., 2009) using L-Anap as the FRET donor (Chatterjee et al., 2013; Zagotta et al., 2016; Dai and Zagotta, 2017). Our results suggest that the intrinsic ligand (1) can act as allosteric modulator of zELK-channel gating like an extrinsic ligand, (2) switches from an antagonist to an agonist during VDP, and (3) moves dynamically during the process of VDP.

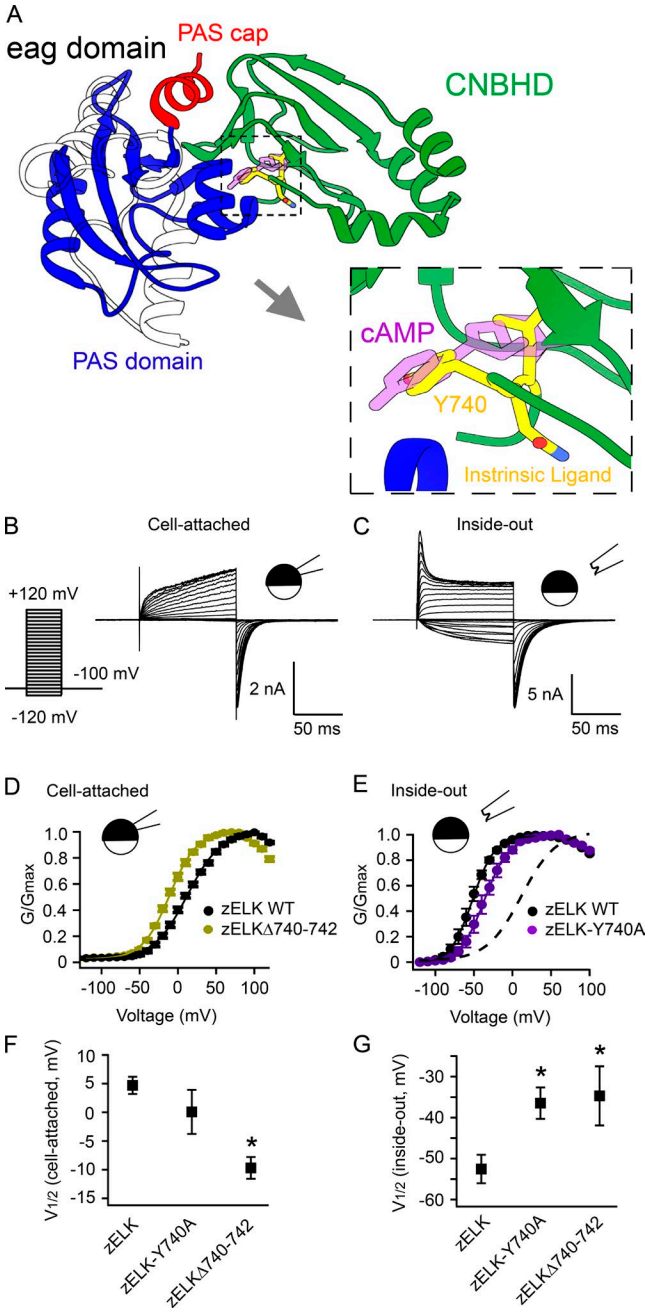

Figure 1. **Mutating and deleting the intrinsic ligand altered the gating of zELK channels. (A)** Ribbon diagram showing the interaction between the eag domain (consisting of the PAS domain and PAS cap) and CNBHD for KCNH channels, based on the cryo-EM structure of rEAG1 channel (Protein Data Bank accession no. 5K7L). Residues of the intrinsic ligand are highlighted in yellow. The position of cAMP in the corresponding structure of mHCN2-CNBD (Protein Data Bank accession no. 1Q5O) is shown in purple. **(B)** Representative I-V current traces of zELK wild-type channels in the cell-attached configuration using the voltage protocol on the left. **(C)** I-V current traces of zELK wild-type channels in the inside-out configuration (15 min after excision, same patch as B). **(D)** Normalized G-V curves for zELK wild-type and Δ740–742 channels in the cell-attached configuration. **(E)** Normalized G-V curves for zELK wild-type and Y740A channels in the inside-out configuration. The dashed line is the G-V curve for zELK wild-type in the cell-attached configuration. **(F)** Summary of the $V_{1/2}$ obtained from experiments related to D. **(G)** Summary of the $V_{1/2}$ obtained from experiments related to E. Data are shown as mean ± SEM (n = 4–5). *, P < 0.05.

Materials and methods

Molecular biology and protein biochemistry

The full-length *Danio rerio* zELK construct (GI: 159570347) was synthesized (Bio Basic) and subcloned into a modified pcDNA3 vector that contained a C-terminal YFP, a T7 promoter, and 3′ and 5′ untranslated regions of a *Xenopus laevis* β-globin gene. Point mutations were made using the Quickchange II XL Site-Directed Mutagenesis kit (Agilent Technologies). The deletions were made using standard overlapping PCR followed by ligation using T4 ligase or Gibson Assembly (New England Biolabs). The sequences

of the DNA constructs were confirmed by fluorescence-based DNA sequencing (Genewiz). The RNA was synthesized in vitro using the HiScribe T7 ARCA mRNA kit (New England Biolabs) or the mMESSAGE mMACHINE T7 ULTRA Transcription kit (ThermoFisher) from the linearized cDNA.

Purification of maltose-binding protein (MBP)–C-linker/CNBHD proteins was done as previously described (Brelidze et al., 2009, 2012). The C-linker/CNBHD proteins from zELK channels (amino acids Q543–L750) with or without Y740–L742 were subcloned into a modified pMalc2T vector (New England Biolabs) containing an N-terminal MBP affinity tag. The proteins were expressed in BL21(DE3) *Escherichia coli* cells and purified on an amylose affinity column (New England Biolabs).

Simultaneous electrophysiology and fluorescence measurements

X. laevis oocytes were prepared as previously described (Varnum et al., 1995). The pANAP plasmid cDNA (~50 nl of 100 ng/ml) containing the orthogonal tRNA/aminoacyl-tRNA synthetase specific to L-Anap (Chatterjee et al., 2013) was injected into the *X. laevis* oocyte nucleus. L-Anap (~50 nl of 1 mM free-acid form; AsisChem) as well as channel mRNA were injected into the cytosolic regions of oocytes separately. 2–4 d after injection, currents were recorded in the cell-attached and inside-out configurations of the patch-clamp technique using an EPC-10 (HEKA Elektronik) or Axopatch 200B (Axon Instruments) patch-clamp amplifier and PATCHMASTER software (HEKA Elektronik). For oocyte patch-clamp recording, the standard bath and pipette saline solutions contained 130 mM KCl, 10 mM HEPES, and 0.2 mM EDTA, pH 7.2. For PCF, 0.5 mM niflumic acid was added to the bath solution and the perfusion solution to remove calcium-activated Cl^- currents. Different concentrations of Co^{2+} were added to the perfusion solution with EDTA eliminated. Borosilicate patch electrodes were made using a P97 micropipette puller (Sutter Instruments). The initial pipette resistance was 0.3–0.7 MΩ for oocyte recordings. Recordings were made at 22–24°C.

VCF simultaneously records fluorescent and current signals in intact oocytes (Fig. S3 A). Our VCF setup integrates a two-electrode voltage-clamp setup (CA-1B high performance oocyte clamp; Dagan), a photomultiplier-based optic system (Cairn Research), and a Xenon lamp on a Nikon FN-S2N upright microscope with a 10× 0.3 numerical aperture objective. The fluorescent filter cube used a 360–390-nm excitation filter, a 430–490-nm emission filter, and a 400-nm long-pass dichroic mirror (Chroma). The bath solution was 130 mM KCl, 10 mM HEPES, and 0.2 mM EDTA, pH 7.2. Both microelectrodes for the two-electrode voltage clamp used 3 M KCl as internal solutions and had an initial pipette resistance of 0.4–2 MΩ.

PCF simultaneously records fluorescence and current signals in inside-out patches. Our PCF setup was performed using a Nikon Eclipse TE2000-E inverted microscope with a 60× 1.2 numerical aperture water immersion objective. Epifluorescence recording of L-Anap was performed with wide-field excitation using a Lambda LS Xenon Arc lamp (Sutter Instruments) and a filter cube containing a 376/30-nm excitation filter and a 485/40-nm emission filter. YFP was measured with a filter cube containing a 490/10-nm excitation filter and a 535/30-nm emission filter. Images were collected with a 100-ms exposure using an Evolve 512 electron-modifying charge-coupling device camera (Photometrics) and MetaMorph software (Molecular Devices). The µFlow Microvolume Perfusion system (ALA Scientific Instruments) was used to change solutions during the experiment. For spectral measurements, images were collected by a spectrograph (model 2150i; Acton Research) on the output port of the microscope and the Evolve 512 electron-modifying charge-coupling device camera. Spectra were recorded by measuring line scans across the patch area and background subtracting using the nonfluorescent region outside of the patch.

Fluorescence anisotropy

Fluorescence anisotropy measurements were performed in a cuvette using a spectrophotometer (Fluorolog 3; HORIBA Jobin Yvon) with Glan-Thompson polarizers. Anisotropy experiments were performed with 488-nm excitation (5-nm slit bandpass) and 512-nm emission (5-nm slit bandpass) as previously described (Rossi and Taylor, 2011; Haitin et al., 2013). An excitation polarizer was positioned in the excitation path directly before the cuvette, and a rotatable emission polarizer was positioned directly after the cuvette. The intensities (I) of polarized emission were measured parallel (II) and perpendicular ($\perp$) to the direction of excitation. The anisotropy was calculated using the following equation: $A = (I_{II} - I_{\perp})/(I_{II} + 2I_{\perp})$. The same fluorescein-labeled peptides were used for the anisotropy experiments as for the electrophysiological recordings.

Data analysis

All data were analyzed using IgoPro (Wavemetrics). Data parameters were expressed as mean ± SEM of n experiments unless otherwise indicated. Statistical significance ($P < 0.05$) was determined by using Student's t test.

The FRET efficiency was calculated using the following equation as previously described (Dai and Zagotta, 2017):

$$FRET_{eff} = \frac{F_{noHH} - F_{HH}}{F_{HH} \times F_{noHH} + F_{noHH} - F_{HH}},$$

where F_{HH} is the normalized fluorescence in the construct with the dihistidine and F_{noHH} is the normalized fluorescence in the absence of the dihistidine. In each case, the F values are the fluorescence measured at metal concentrations that saturate the binding sites normalized by the fluorescence in the absence of metal, e.g., $F_{HH} = fl(\text{metal})/fl(\text{no metal})$. This equation of calculating FRET efficiency assumes that the decrease in F_{noHH} is caused by nonspecific energy transfer such as solution quenching or FRET to a metal ion bound to an endogenous metal-binding site. The distance (R) between L-Anap and the metal ion was calculated using the Förster equation $R = R_0(1/FRET_{eff} - 1)^{1/6}$, where R_0 is the Förster distance for FRET.

The channel G-V curves were measured from the instantaneous tail currents at –100 mV as a function of the voltage of the main pulse. They were fit with a Boltzmann equation:

$$I = I_{min} + (I_{max} - I_{min})/(1 + \exp[(V_{1/2} - V)/V_s]),$$

where I_{max} is the maximum tail current after steps to +100 mV, I_{min} is the minimum tail current after hyperpolarizing voltage steps,

V is the membrane potential, $V_{1/2}$ is the potential for half-maximal activation, and V_s is the slope factor.

Online supplemental material

Fig. S1 shows that the S499T mutation abolished the inactivation of zELK channels. Fig. S2 shows a summary of the time constants of the tail currents. Fig. S3 shows the effects of the intrinsic-ligand peptide. Fig. S4 shows a comparison of PCF and VCF. Fig. S5 shows properties of zELK-N741Anap channels. Fig. S6 shows successful incorporation of Anap for zELKΔPAS cap-N741TAG, L682H, and G684H channels.

Results

This paper elucidates the dynamic regulation of a *D. rerio* ELK channel by its intrinsic ligand. The intrinsic ligand of zELK channels consists of a tyrosine (Y740), an asparagine (N741), and a leucine (L742) at the C-terminal end of the CNBHD and is situated in a binding pocket analogous to the cyclic nucleotide-binding pocket in CNG and HCN channels. Compared with the cyclic nucleotide bound to the CNBD of CNG and HCN channels, the tyrosine mimics the purine ring of the cyclic nucleotide, whereas the leucine occupies the position of the phosphoribose group (Fig. 1 A). Importantly, the intrinsic ligand is located in the interface between the N-terminal eag domain and the C-terminal CNBHD (Fig. 1 A).

zELK channels are regulated by the intrinsic ligand

We used patch-clamp recording to characterize the gating of zELK channels expressed in *X. laevis* oocytes. The G-V curve was measured from the peak tail-current amplitude at −100 mV immediately after a 100-ms depolarization to voltages between −120 and +120 mV (Fig. 1 B). Previously, we showed that zELK channels exhibited a dramatic run-up after patch excision. The currents after run-up exhibited an ∼60-mV hyperpolarizing shift in the G-V curve, an increase in the maximal conductance, and inactivation at very depolarized voltages (>+60 mV; Fig. 1 C). This inactivation was not caused by ion accumulation in the patch electrode and was unaffected by the current amplitude (not depicted). This type of inactivation is similar to the inactivation observed in mouse ELK2 channels (Trudeau et al., 1999). Furthermore, a single mutation zELK-S499T near the pore region was able to eliminate this inactivation, whereas it left the VDP and the run-up intact (Fig. S1). In addition, this run-up was complete 10–20 min after excision and could be prevented by supplementing the intracellular solution with MgATP (Dai and Zagotta, 2017). Run-up was probably caused by the inhibition of zELK channels by $PI(4,5)P_2$, which is hydrolyzed in the absence of MgATP upon patch excision (Li et al., 2015; Dai and Zagotta, 2017).

We found the phenotype associated with mutating the intrinsic ligand differed depending on the patch configuration. In the cell-attached patch configuration, deleting the intrinsic ligand (zELKΔ740–742) shifted the G-V curve to more hyperpolarized voltages relative to wild-type zELK (Fig. 1, D and F). This suggests that the intrinsic ligand was inhibitory for voltage-dependent channel opening. In contrast, in the inside-out configuration after run-up, zELKΔ740–742 and zELK-Y740A channels shifted the G-V curve to more depolarized voltages, consistent with our previous report (Brelidze et al., 2012), indicating that the intrinsic ligand was promoting channel opening (Fig. 1, E and G). These results show that mutating the intrinsic ligand has opposite effects before and after run-up.

VDP of zELK channels is regulated by the intrinsic ligand

We have previously shown that zELK channels undergo VDP, which manifests in three ways (Dai and Zagotta, 2017): (1) a double-exponential increase in the current elicited by depolarizing voltages (Fig. 2 A, left); (2) a shift of the G-V curve to more hyperpolarized voltages and a significant increase in maximum conductance in response to a 500-ms, +60-mV depolarizing prepulse (Fig. 2 B, left); and (3) a slowing of the tail current with prolonged depolarizing pulses (Fig. 2 C, left; and Fig. S2). These behaviors could be quantitatively explained by a model for VDP in which the channel undergoes a slow, voltage-independent transition from the open state to a mode with more favorable opening (Dai and Zagotta, 2017).

The processes of VDP and run-up are clearly related. Both VDP and run-up exhibited a large hyperpolarizing shift in the voltage dependence of activation (Fig. 2 B) and an increase in the maximum open probability. In addition, VDP was lost after patch excision unless the intracellular solution was supplemented with MgATP. These experiments suggest that $PI(4,5)P_2$ is a required cofactor for VDP, maintaining the channel in the resting mode at hyperpolarized potentials.

Is the intrinsic ligand involved in VDP? All three features of VDP were eliminated or significantly attenuated by deletion of the intrinsic ligand (Fig. 2). zELKΔ740–742 channels did not exhibit a slow component for activation and displayed some inactivation at very depolarized voltages (Fig. 2 A, right). In addition, zELKΔ740–742 channels exhibited less shift of the G-V curve, no increase in maximum conductance, and less slowing of channel deactivation with depolarizing prepulses (Fig. 2, B and C; and Fig. S2). The intrinsic ligand seems to be required for the channel to adopt the resting unpotentiated state. Y740A in the intrinsic ligand similarly attenuated VDP (Fig. 2, D and E; and Fig. S2). Furthermore, because the intrinsic ligand is located at the eag domain–CNBHD interface and deleting the N-terminal eag domain almost eliminated VDP (Dai and Zagotta, 2017), we made a zELK channel with both the eag domain and the intrinsic ligand deleted (zELKΔeag, Δ740–742). We found zELKΔeag, Δ740–742 channels did not further alter VDP compared with zELKΔeag channels (Fig. 2, D and E; $P > 0.05$). These results suggest that the intrinsic ligand modulates VDP perhaps because it regulates the eag domain–CNBHD rearrangement.

As we found with the different patch configurations, the phenotype of mutating the intrinsic ligand was different before and after VDP. Without a depolarizing prepulse, deletion of the intrinsic ligand shifted the G-V curve to more hyperpolarized voltages (Fig. 1, D and F). With a depolarizing prepulse, however, the deletion mutant shifted the G-V curve to more depolarized voltages (wild-type zELK, $V_{1/2} = -49 \pm 1.5$ mV; zELKΔ740–742, $V_{1/2} = -37 \pm 1.5$ mV [$n = 8$]). Based on these results, we propose that the intrinsic ligand acts as an inhibitor in the resting mode and as an activator in the potentiated mode. Collectively, these results indicate that VDP is regulated by the intrinsic ligand and, reciprocally, the effect of the intrinsic ligand is regulated by VDP.

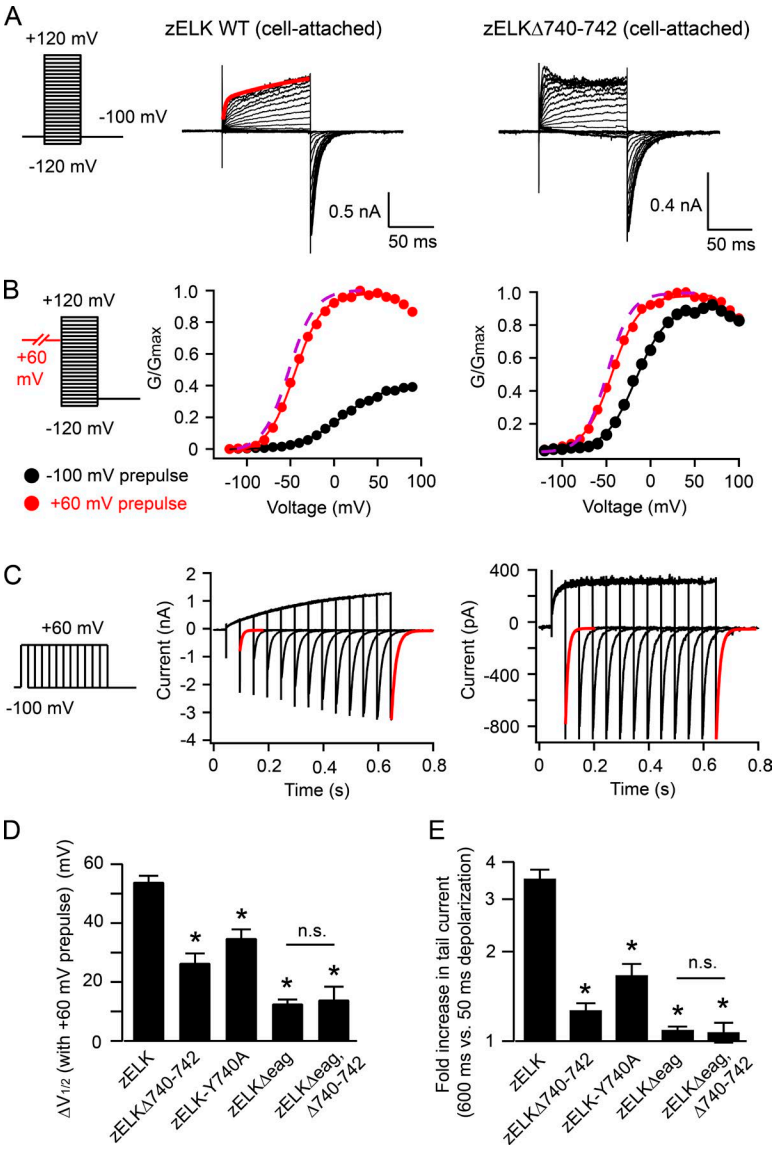

Figure 2. **VDP was attenuated by mutating the intrinsic ligand. (A)** Representative I-V current traces for zELK wild-type and Δ740–742 channel activation in the cell-attached configuration using the voltage protocol on the left. The red trace is the double-exponential fit to the current elicited by the +120-mV voltage pulse (τ1 = 3 ms and τ2 = 130 ms). **(B)** Normalized G-V curve of zELK wild-type and Δ740–742 channel activation with and without a 500-ms, +60-mV prepulse. The purple dashed curves indicate the G-V curves of zELK wild-type and Δ740–742 channels after run-up caused by patch excision, highlighting the similar degree of hyperpolarizing shift compared with that caused by the +60-mV prepulse. **(C)** Current traces of zELK wild-type and Δ740–742 channels elicited by a voltage protocol with increasing durations of a +60-mV pulse (left). For the wild-type channels, τ of the tail current (red traces) increased from 8 to 17 ms. For zELKΔ740–742 channels, τ of the tail current (red traces) changed from 10 to 13 ms. **(D)** Summary of the changes in $V_{1/2}$ for different zELK channels with and without the +60-mV prepulse using the protocol in B. n.s., not statistically significant. **(E)** Summary of the fold increase in the tail current amplitude of zELK channels using the protocol in C; mean ± SEM (n = 4–8). *, P < 0.05.

Exogenous intrinsic-ligand peptide can bind and regulate zELK channels

Does the regulation of the intrinsic ligand require covalent attachment to the C helix of the CNBHD? To address this question, we used an intrinsic-ligand peptide with the sequence ILTYNLR. This peptide contains amino acids 696–702 of mouse EAG1 (mEAG1) and is highly similar to amino acids 737–743 of zELK channels. Surprisingly, application of 100 µM mEAG1 peptide to inside-out patches rescued the wild-type gating behavior of zELKΔ740–742 channels (Figs. 3 and S3). Similar to the effect of deleting the intrinsic ligand in different patch-clamp configurations (Fig. 1, D–G), the mEAG1 peptide produced opposite effects for zELK channels depending on the different modes of channel activation. We found that applying 100 µM mEAG1 peptide to inside-out patches containing zELKΔ740–742 channels shifted the G-V curve to more depolarized voltages in the presence of MgATP (Fig. 3 A). In addition, the pronounced slow component of activation and the slowing of deactivation caused by long depolarizing pulses of wild-type channels were rescued after the addition of mEAG1 peptide (Fig. S3, A and B). In contrast, the peptide shifted the G-V curve to more hyperpolarized voltages in the absence of MgATP (Fig. 3 B). The same peptide did not affect the gating of wild-type zELK channels (Fig. S3 C). Applying the intrinsic-ligand peptide from hERG1 channels (#857–863) did not produce an appreciable amount of modulation for zELKΔ740–742 channels regardless of MgATP (Fig. S3, A, D, and E). The main difference between the mEAG1 and hERG1 peptide is that hERG1 peptides possess a phenylalanine (F) instead of a tyrosine (Y) for mEAG1 peptide. This difference might partially explain why the hERG1 peptide is unable to modulate zELKΔ740–742 channels. Collectively, these results indicate that the intrinsic ligand can regulate the channel gating without its attachment to the C helix of the CNBHD.

To more directly show that the intrinsic-ligand peptide is able to bind to the CNBHD, we performed fluorescence anisotropy experiments using fluorescein-labeled intrinsic-ligand peptides. Fluorescence anisotropy reports binding by measuring the degree of polarized emissions with polarized excitation (Rossi and Taylor, 2011). A small fluorophore-labeled peptide in solution typically has a high degree of tumbling or rotational motion, producing low anisotropy. When the fluorophore-labeled peptide binds to a large protein,

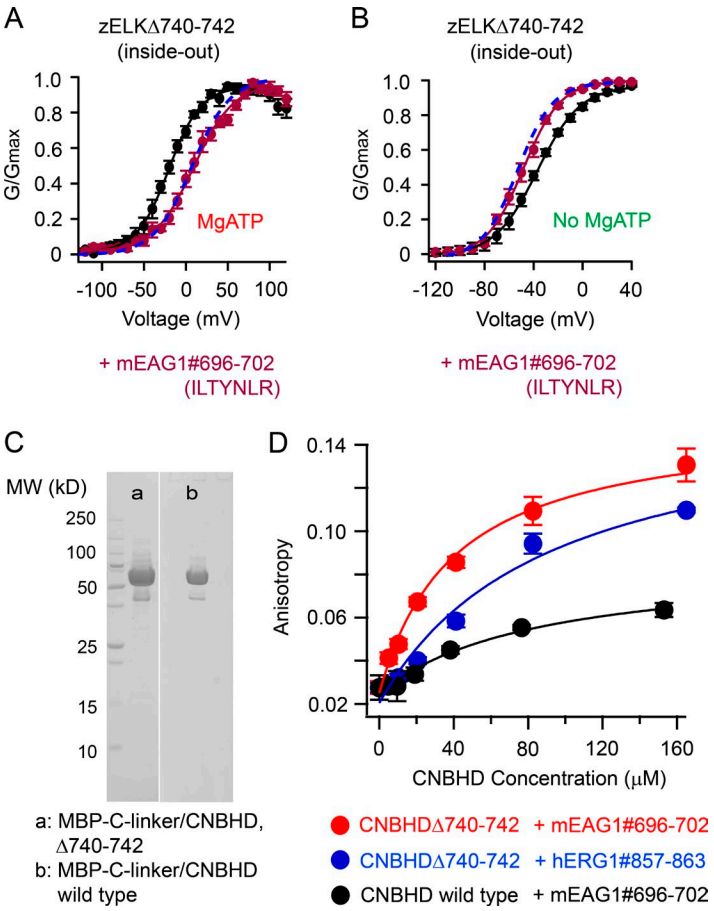

Figure 3. **Intrinsic-ligand peptide bound to the CNBHD of zELK channels and modulated the channel gating. (A and B)** G-V curves of zELKΔ740–742 channels before and after applying the intrinsic ligand peptide in the inside-out patch configuration in the presence (A) or absence (B) of MgATP. The dashed lines are G-V curves for zELK wild-type in the presence (A) or absence (B) of MgATP as references. **(C)** Coomassie-stained gel showing purified C-linker/CNBHD and C-linker/CNBHDΔ740–742 with MBP fused to the amino-terminal end. **(D)** Fluorescence anisotropy of the mEAG1 and the hERG1 intrinsic-ligand peptides with an increasing concentration of wild-type or Δ740–742 CNBHD protein (mean ± SEM, n = 4–5).

however, the rotational motion of the fluorophore will decrease and the anisotropy will increase (Rossi and Taylor, 2011). In this way, we can measure the binding affinity of the peptide to a larger protein.

We expressed and purified the isolated CNBHD of zELK channels in *E. coli* and studied the binding of the exogenously applied intrinsic ligand in vitro using anisotropy. Wild-type or Δ740–742 C-linker/CNBHD fragments were purified as MBP fusions using an amylose affinity column. The fusion proteins were monodisperse and exhibited the expected molecular weights on SDS-polyacrylamide gels (Fig. 3 C). We found, at a constant concentration of the intrinsic-ligand peptide (mEAG1#696–702, 20 nM), increasing the concentration of CNBHDΔ740–742 produced elevated anisotropy (Fig. 3 D). Fitting with a Langmuir isotherm indicated an apparent affinity of 37 μM for this binding. The hERG1#857–863 intrinsic ligand peptide similarly bound to CNBHDΔ740–742 but exhibited a lower affinity (90 μM). This lower affinity of the hERG1 peptide could partially explain the lack of regulation of zELKΔ740–742 channels in inside-out patch-clamp recordings. Compared with intrinsic-ligand binding to CNBHDΔ740–742, the binding to wild-type CNBHD was detectable but with a lower affinity (85 μM) and efficacy (Fig. 3 D). These data suggest that the exogenously applied intrinsic ligand could bind to the ligand-binding pocket of the CNBHD and compete with the endogenous intrinsic ligand of the wild-type CNBHD. The endogenous intrinsic ligand of the wild-type CNBHD might be mobile, which allows the exogenously applied ligand to insert into the binding cavity when the endogenous ligand is displaced.

VCF reveals changes in the environment of the intrinsic ligand during VDP

From the above experiments, we hypothesized that the intrinsic ligand is dynamic during VDP of zELK channels. VCF (Fig. S4 A) was used to test this hypothesis. VCF allows us to simultaneously record the ionic current with two-electrode voltage clamp and structural rearrangements in the channel with site-specific fluorescence using *X. laevis* oocytes (Mannuzzu et al., 1996). We incorporated a fluorescent noncanonical amino acid L-Anap into the intrinsic ligand and used the property of L-Anap that it alters its emission in response to environmental changes (Chatterjee et al., 2013; Kalstrup and Blunck, 2013; Sakata et al., 2016). L-Anap was incorporated using the amber stop-codon (TAG) suppression strategy, where the channel containing TAG at the site of interest was coexpressed with an orthogonal tRNA/aminoacyl-tRNA synthetase pair evolved for L-Anap incorporation (Chatterjee et al., 2013; Kalstrup and Blunck, 2013; Dai and Zagotta, 2017). L-Anap was incorporated at N741 in the intrinsic ligand as well as L738 and E744 flanking the intrinsic ligand (Fig. 4 A). Key residues of the intrinsic ligand (Y740 and L742) were left intact to maintain the wild-type gating behavior.

VCF was performed for zELK-L738Anap, N741Anap, and E744Anap channels. zELK-L738Anap channels showed no change in Anap fluorescence during a +60-mV depolarization (Fig. 4 B). The activation of L738Anap channel still has a slow component corresponding to VDP, with a time constant of 90 ± 3 ms. In addition, for L738Anap channels, the time constant for the tail

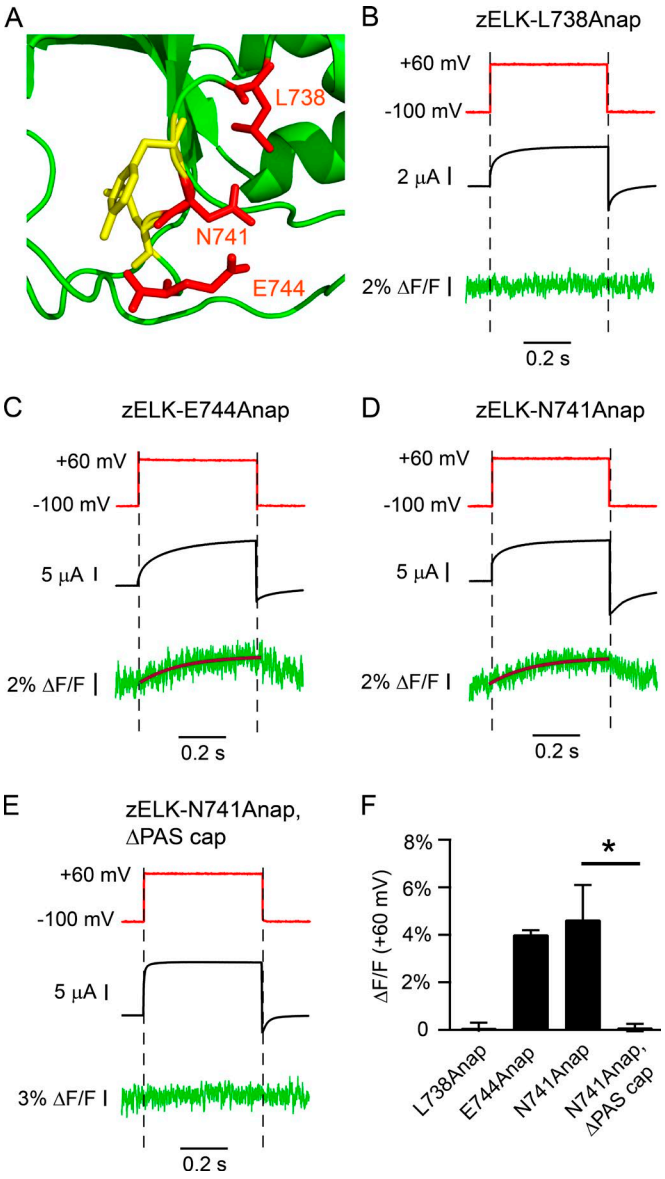

Figure 4. **VCF revealed voltage-dependent changes of Anap fluorescence during VDP of zELK channels. (A)** Ribbon diagram highlighting the residues within or flanking the intrinsic ligand of zELK that were mutated to L-Anap for VCF experiments. **(B–E)** Simultaneous Anap fluorescence measurements and two-electrode voltage-clamp recordings showing the kinetic change of Anap fluorescence during the depolarizing pulses for zELK-L738Anap (B), zELK-E744Anap (C), zELK-N741Anap (D), and zELK-N741Anap, ΔPAS cap (E) channels. The fluorescence traces are shown as the mean of 6–13 repetitive measurements using the same oocyte. **(F)** Summary of the percent increase in Anap fluorescence induced by depolarization for constructs in B–E (increase in fluorescence at the end of the +60-mV pulse versus that at −100 mV); mean ± SEM (n = 3–5). *, P < 0.05.

current with a 600-ms prepulse is >50% greater than that with a 50-ms prepulse, consistent with the presence of VDP (unpublished data). However, zELK-N741Anap and zELK-E744Anap channels exhibited a noticeable increase in Anap fluorescence with depolarization and a recovery in Anap fluorescence after repolarization (Fig. 4, C, D, and F). The kinetics of the fluorescence increase during depolarization were comparable to the kinetics of the slow component of activation corresponding to VDP. The time constants for the increase in Anap fluorescence with depolarization were 174 ± 22 ms for E744Anap and 137 ± 23 ms for N741Anap, whereas the time constants for VDP were 146 ± 8 ms for E744Anap and 153 ± 13 ms for N741Anap. These data indicate that a structural rearrangement occurs during VDP that changes the environment of the intrinsic ligand.

Since we have shown that the effect of the intrinsic ligand is dependent on the N-terminal eag domain (Fig. 2, D and E), we asked whether mutations of the eag domain would affect the voltage-dependent change in Anap fluorescence. To test this, we made a construct of zELK-N741Anap with the first 26 amino acids of the eag domain (PAS cap) removed. For hERG channels, removing the PAS cap produced almost identical effects to deleting the whole eag domain (Morais Cabral et al., 1998; Wang et al., 2000; Muskett et al., 2011; Ng et al., 2011). We found that removing the PAS cap of zELK N741Anap channels greatly reduced the VDP and abolished the depolarization-induced increase in Anap fluorescence (Fig. 4, E and F), suggesting that the rearrangement of the intrinsic ligand or neighboring regions requires the N-terminal PAS cap domain, similar to VDP.

Transitional metal ion FRET (tmFRET) measurements detect voltage-dependent movement of the intrinsic ligand

To determine whether the intrinsic ligand is actually moving during VDP and quantify the degree of movement, we used tmFRET. tmFRET uses FRET between a fluorophore and a transition metal cation to precisely measure short-range intramolecular distances (Taraska et al., 2009; Aman et al., 2016; Zagotta et al., 2016; Dai and Zagotta, 2017). Nonfluorescent transition metal cations such as Ni^{2+}, Co^{2+}, and Cu^{2+} act as FRET acceptors, quenching the fluorescence of donor fluorophores in a highly distance-dependent manner. Because transition metal ions have a small extinction coefficient, tmFRET has a working distance range of ∼10–20 Å, much shorter than that of traditional FRET methods. We used L-Anap at position N741 in the intrinsic ligand as the tmFRET donor and Co^{2+} coordinated by an engineered dihistidine motif (L682H,G684H) in the β-roll region of the CNB HD as the tmFRET acceptor (Fig. 5 A). For the L-Anap/Co^{2+}-dihistidine FRET pair, the Förster distance (R_0), producing 50% FRET efficiency, is ∼13 Å (Dai and Zagotta, 2017).

tmFRET was combined with PCF (Fig. S4 B), which is a technique that simultaneously measures the fluorescence and current from channels in an inside-out patch while controlling the membrane voltage and intracellular solution (Zheng and Zagotta, 2003). zELK-N741Anap,L682H,G684H was constructed as a C-terminal YFP fusion to independently measure the number of channels in inside-out patches. We found that the L-Anap fluorescence intensity in patches was linearly correlated with the YFP intensity, indicating specific incorporation of L-Anap into the channel (Fig. 5 B). zELK-N741Anap,L682H,G684H channels exhibited similar electrophysiological properties to wild-type channels (Fig. S5, A–C).

The tmFRET efficiency was measured by the decrease in donor fluorescence upon addition of increasing concentrations of the metal (Co^{2+}) acceptor (Fig. S5 D). The measured FRET efficiency can be affected by nonspecific decreases in fluorescence that do not involve FRET with the metal-bound dihistidine (HH) motif. These nonspecific decreases in donor fluorescence can be

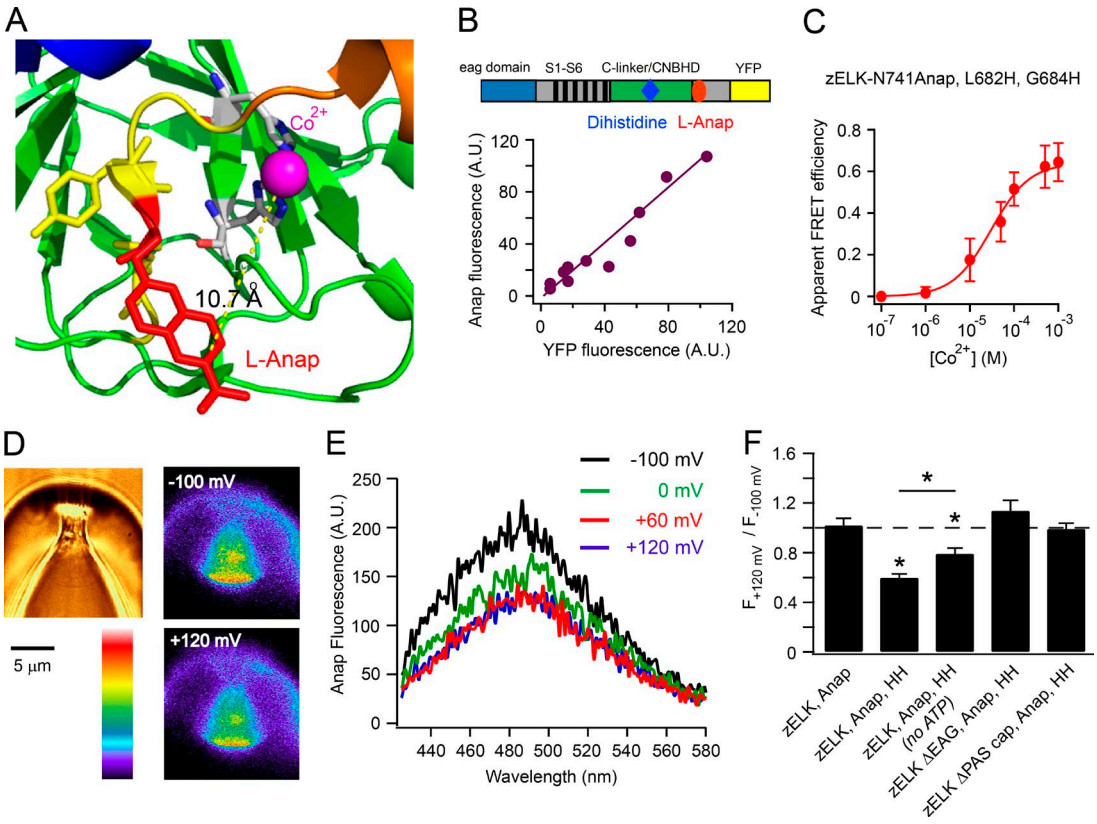

Figure 5. **PCF/tmFRET revealed the movement of the intrinsic ligand relative to CNBHD. (A)** Ribbon diagram showing the incorporation of L-Anap (red) within the intrinsic ligand and Co^{2+} coordinated by a dihistidine pair in the β-roll region of the CNBHD of zELK channels. **(B)** Relationship of Anap fluorescence versus YFP fluorescence measured by PCF for zELK-N741Anap,L682H,G684H channels. The illustration at the top shows the positions of Anap and YFP in the sequence. A.U., arbitrary units. **(C)** Apparent tmFRET efficiency measured at different concentrations of Co^{2+} using PCF at −100 mV and in the presence of MgATP for zELK-N741Anap,L682H,G684H channels. The smooth curve is the fit of Langmuir isotherm, Apparent $FRET_{eff.} = FRET_{eff}[Co^{2+}]/(K_{1/2} + [Co^{2+}])$, with the following parameters: $FRET_{eff} = 0.64$, $K_{1/2} = 30.3$ µM. **(D)** Representative heatmaps of PCF images of zELK-N741Anap,L682H,G684H channels in the presence of 1 mM Co^{2+} and 2 mM MgATP at −100-mV or +120-mV voltages. The brightfield view of the same patch is shown on the left. The Anap fluorescence intensity of the patch membrane at +120 mV decreased 34% compared with that at −100 mV. **(E)** Spectra of L-Anap emission at different voltages from a patch containing zELK-N741Anap,L682H,G684H channels in the presence of 1 mM Co^{2+} and 2 mM MgATP. **(F)** Summary graph showing the Anap fluorescence at +120 mV relative to the fluorescence at −100 mV for the various zELK constructs and conditions indicated; mean ± SEM (n = 4–5). *, $P < 0.05$. Inside patches were in the bath solution supplemented with MgATP unless otherwise indicated.

measured from channels without the dihistidine (Dai and Zagotta, 2017; zELK-N741Anap in this experiment) and used to calculate the apparent FRET efficiency (Fig. 5 C). The tmFRET efficiency at saturating (1 mM) Co^{2+} concentration for zELK-N741Anap,L-682H,G684H channels at −100 mV was 0.64, corresponding to a distance of 11.8 Å, which is compatible with the estimated distance (10.7 Å) in the homology model of zELK using the solved structures of EAG1 channels (Fig. 5, A and C; Haitin et al., 2013; Whicher and MacKinnon, 2016).

We next measured the tmFRET at different voltages (Fig. 5, D and E). We found that with 1 mM Co^{2+} and MgATP in the bath, the Anap fluorescence was significantly decreased at +120 mV compared with −100 mV (Fig. 5 D). This decrease was not observed in the absence of a Co^{2+}-binding site (Fig. 5 F), indicating that the decrease was not caused by an environmental change in N741Anap, but instead was caused by specific tmFRET with the Co^{2+} site. The small increase in N741Anap fluorescence caused by the depolarization observed using VCF (Fig. 4 D) was not detected here, possibly because of the small size of the increase or a change in the intracellular environment after patch excision. We also measured the spectrum of Anap emission from the patch using a spectrograph attached to the microscope. We found the peak intensity of Anap emission decreased with depolarizing voltages without a change in the peak emission wavelength, consistent with a FRET mechanism (Fig. 5 E). The higher FRET efficiency at +120 mV (0.79) relative to −100 mV (0.64) indicates that the intrinsic ligand and β-roll region of CNBHD move closer together by ∼1.4 Å because of the depolarizing voltage pulse. In contrast, the decrease in Anap fluorescence at +120 mV was significantly less pronounced in the absence of MgATP (Fig. 5 F). In addition, removing the N-terminal eag domain or PAS cap eliminated this depolarization-induced decrease in fluorescence (Fig. 5 F). These results suggest a voltage-dependent movement of the intrinsic ligand, which is dependent on MgATP and the eag domain, similar to VDP.

The rearrangement of the intrinsic ligand has the kinetics of VDP

Using PCF, the kinetics of intrinsic ligand movement can also be measured simultaneously with ionic-current recordings. Here, we measured the kinetics of the changes in tmFRET in the

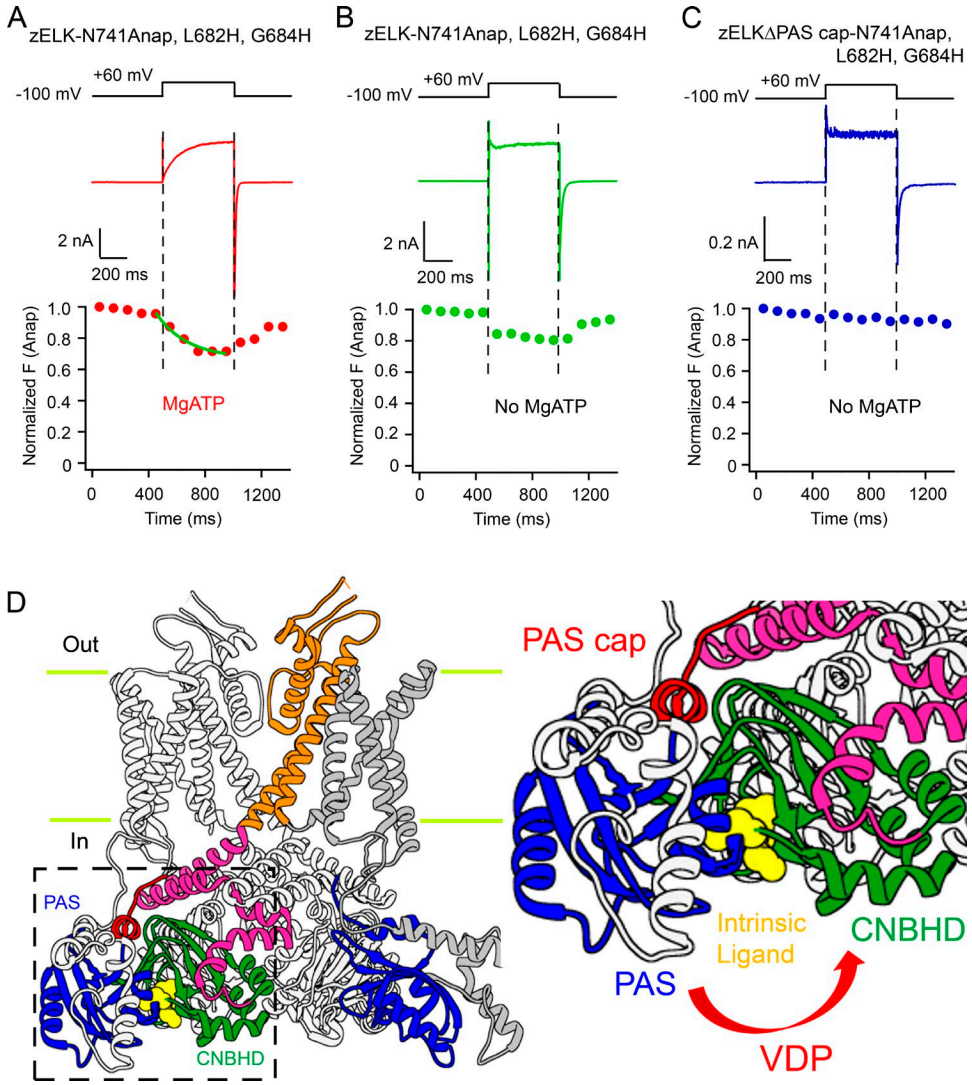

Figure 6. **Kinetic tmFRET measurement demonstrated the movement of the intrinsic ligand during VDP. (A–C)** Simultaneous tmFRET and current measurements using PCF for zELK-N741Anap,L682H,G684H channels with 1 mM Co^{2+} in the presence (A) or absence (B) of 2 mM MgATP or after deleting the PAS cap (C). The green trace in A is the single-exponential fit with a τ of 219 ms. **(D)** Ribbon diagram showing the full-length KCNH channel (rEAG1; Protein Data Bank accession no. 5K7L), highlighting the intrinsic ligand (in yellow) and the intersubunit interaction between the eag domain (in blue) and CNBHD (in green). Only two subunits are shown for simplicity except that the C-linker region (in magenta) is displayed in a tetrameric assembly. Ribbon diagram is the amplified view of the structure in the dashed-line rectangle. The red arrow indicates the eag domain–CNBHD rearrangement associated with the VDP.

presence of 1 mM Co^{2+} for zELK-N741Anap,L682H,G684H channels during voltage steps to +60 mV. In the presence of MgATP, the ionic current increased gradually, whereas the Anap fluorescence decreased with a time course matching that of the ionic current (Fig. 6 A). The time constant for this decrease in Anap fluorescence was 202 ± 27 ms (n = 5), close to the time constant for the development of VDP (162 ± 16 ms; n = 5).

In the absence of MgATP, the ionic current increased rapidly after the +60-mV depolarization (with a small amount of inactivation observed); at the same time, Anap fluorescence decreased rapidly and stayed unchanged during the depolarization (Fig. 6 B). Interestingly, when we deleted the PAS cap from zELK-N741Anap,L682H,G684H channels, the small decrease in Anap fluorescence was eliminated in the absence of MgATP (Fig. 6 C). For this PAS cap–deleted construct, we also confirmed that Anap was successfully incorporated (Fig. S6). Together, these results indicate that the intrinsic ligand is dynamically rearranging its position relative to the CNBHD during the zELK channel gating, which requires the eag domain and is regulated by MgATP. We suggest that this rearrangement of the intrinsic ligand is facilitating channel opening and is promoted by the eag domain–CNBHD rearrangement that is associated with VDP.

Discussion

In this paper, we demonstrate that the intrinsic ligand can act as an allosteric modulator of zELK potassium channels, switching from an antagonist to an agonist during VDP. Furthermore, we show that the intrinsic ligand moves dynamically during voltage-dependent activation. This movement has a similar time course to VDP and, like VDP, is dependent on MgATP and the N-terminal eag domain. We propose that the intrinsic ligand switches from

an antagonist to an agonist as a result of a slow rearrangement of the eag domain–CNBHD interaction during VDP (Fig. 6 D).

How is the movement of the intrinsic ligand dependent on membrane voltage? Indeed, the S4 voltage sensor domain is far away from the intracellular intrinsic ligand. Several pathways are possible for allowing the voltage signal to be transmitted to the C-terminal end of the CNBHD. The intracellular domains could sense the movement of the voltage sensor. This coupling could occur through direct interactions between the PAS cap and the S4–S5 linker as suggested by the recent hERG structure (Wang and MacKinnon, 2017). Alternatively, the S4–S5 linker could directly interact with the C linker and detect movement of the S4, as suggested by functional studies and recent cryo–electron microscopy (cryo-EM) structures of EAG, HCN, and CNG channels (Fig. 6 D; Decher et al., 2004; Prole and Yellen, 2006; Kwan et al., 2012; Whicher and MacKinnon, 2016; Li et al., 2017; Wang and MacKinnon, 2017). However, our previous results suggest that VDP is primarily coupled to pore opening, not voltage sensor movement (Dai and Zagotta, 2017). This coupling could occur through an interaction between the PAS cap and the C linker as supported by the cryo-EM structures of EAG and hERG channels (Fig. 6, D and E; Whicher and MacKinnon, 2016; Wang and MacKinnon, 2017). Finally, the movement of the S6 inner helix during voltage-dependent channel opening could transduce the voltage signal to the C linker/CNBHD. The bottom line is that the membrane voltage signal can be transmitted from the focused electric field of the plasma membrane to the intrinsic ligand that is almost 50 Å away.

We find that the intrinsic ligand has two distinct effects on zELK channel gating. We show that with a short 100-ms depolarization, the effect of the same intrinsic-ligand mutation on zELK channels was dependent on patch-clamp configurations. In the normal cell-attached mode, the intrinsic ligand is inhibitory, whereas after excision and $PI(4,5)P_2$ depletion, the intrinsic ligand is excitatory. Furthermore, the intrinsic ligand can modulate the gating of KCNH channels as a peptide fragment without its covalent linkage to the CNBHD. Similarly, this modulation of the KCNH channel gating by the intrinsic-ligand peptide was either inhibitory or excitatory, depending on the mode of the channel (with or without ATP-dependent $PI(4,5)P_2$ synthesis in the inside-out patch). In other words, during zELK channel gating, the intrinsic ligand slowly switches from an antagonist in the resting mode to an agonist in the potentiated mode during VDP.

Previous work has shown that the intrinsic ligand exhibits diverse effects on different KCNH channels. Mutating the intrinsic ligand produced either potentiation or inhibition for channel activation, depending on the channel type or the specific manipulations of the intrinsic ligand (Brelidze et al., 2012; Marques-Carvalho et al., 2012; Zhao et al., 2017). In hERG channels, mutating the intrinsic ligand only produced an acceleration of channel deactivation but no effects on the steady-state voltage-dependent activation (Brelidze et al., 2013). These results indicate that the intrinsic ligand regulates the gating of all three KCNH channel subfamilies, EAG, ERG, and ELK, but the regulation is diverse for the different channel types and may depend on the recording configuration (whole oocyte vs. excised patch).

Finally, this work shows how the combination of VCF and PCF/tmFRET can be used to illuminate a conformational change of a protein domain. The fluorescent noncanonical amino acid L-Anap was effectively used as an environmentally sensitive fluorophore as well as a tmFRET donor. A change in fluorescence recorded using VCF gives detailed information about the kinetic movement of an individual domain but little information about the nature of the movement. In contrast, a change in tmFRET provides precise information about the small distance changes between FRET donors and acceptors. The integration of these two techniques provides a powerful way to study conformational changes of ion channels.

Acknowledgments

We thank Drs. Sharona Gordon, Bertil Hille, Michael Puljung, and John Bankston for advice and support; Yoni Haitin, Anne Carlson, and Teresa Aman for pilot experiments; Galen Flynn, Eric Evans, and Jacob Morgan for comments on the manuscript; and Ximena Opitz-Araya for technical support.

This work was supported by the National Institute of Mental Health (grant R01MH102378 to W.N. Zagotta) and by the National Eye Institute of the National Institutes of Health (grant R01EY010329 to W.N. Zagotta).

The authors declare no competing financial interests.

Author contributions: G. Dai conceptualized research, designed and performed experiments, analyzed data, and made figures. Z.M. James performed protein purification, assisted with fluorescence anisotropy, analyzed data, and made figures. W.N. Zagotta conceptualized research, designed experiments, performed pilot experiments, and supervised the project. G. Dai and W.N. Zagotta wrote the manuscript.

Richard W. Aldrich served as editor.

Submitted: 29 December 2017
Accepted: 28 February 2018

References

Aman, T.K., S.E. Gordon, and W.N. Zagotta. 2016. Regulation of CNGA1 Channel Gating by Interactions with the Membrane. *J. Biol. Chem.* 291:9939–9947. https://doi.org/10.1074/jbc.M116.723932

Bean, B.P. 1989. Neurotransmitter inhibition of neuronal calcium currents by changes in channel voltage dependence. *Nature.* 340:153–156. https://doi.org/10.1038/340153a0

Brelidze, T.I., A.E. Carlson, and W.N. Zagotta. 2009. Absence of direct cyclic nucleotide modulation of mEAG1 and hERG1 channels revealed with fluorescence and electrophysiological methods. *J. Biol. Chem.* 284:27989–27997. https://doi.org/10.1074/jbc.M109.016337

Brelidze, T.I., A.E. Carlson, B. Sankaran, and W.N. Zagotta. 2012. Structure of the carboxy-terminal region of a KCNH channel. *Nature.* 481:530–533. https://doi.org/10.1038/nature10735

Brelidze, T.I., E.C. Gianulis, F. DiMaio, M.C. Trudeau, and W.N. Zagotta. 2013. Structure of the C-terminal region of an ERG channel and functional implications. *Proc. Natl. Acad. Sci. USA.* 110:11648–11653. https://doi.org/10.1073/pnas.1306887110

Chatterjee, A., J. Guo, H.S. Lee, and P.G. Schultz. 2013. A genetically encoded fluorescent probe in mammalian cells. *J. Am. Chem. Soc.* 135:12540–12543. https://doi.org/10.1021/ja4059553

Craven, K.B., and W.N. Zagotta. 2006. CNG and HCN channels: two peas, one pod. *Annu. Rev. Physiol.* 68:375–401. https://doi.org/10.1146/annurev.physiol.68.040104.134728

Dai, G., and W.N. Zagotta. 2017. Molecular mechanism of voltage-dependent potentiation of KCNH potassium channels. *eLife.* 6:e26355. https://doi.org/10.7554/eLife.26355

Decher, N., J. Chen, and M.C. Sanguinetti. 2004. Voltage-dependent gating of hyperpolarization-activated, cyclic nucleotide-gated pacemaker

channels: molecular coupling between the S4-S5 and C-linkers. *J. Biol. Chem.* 279:13859–13865. https://doi.org/10.1074/jbc.M313704200

Elinder, F., R. Männikkö, S. Pandey, and H.P. Larsson. 2006. Mode shifts in the voltage gating of the mouse and human HCN2 and HCN4 channels. *J. Physiol.* 575:417–431. https://doi.org/10.1113/jphysiol.2006.110437

Fesenko, E.E., S.S. Kolesnikov, and A.L. Lyubarsky. 1985. Induction by cyclic GMP of cationic conductance in plasma membrane of retinal rod outer segment. *Nature.* 313:310–313. https://doi.org/10.1038/313310a0

Ganetzky, B., G.A. Robertson, G.F. Wilson, M.C. Trudeau, and S.A. Titus. 1999. The eag family of K^+ channels in Drosophila and mammals. *Ann. N. Y. Acad. Sci.* 868:356–369. https://doi.org/10.1111/j.1749-6632.1999.tb11297.x

Gianulis, E.C., Q. Liu, and M.C. Trudeau. 2013. Direct interaction of eag domains and cyclic nucleotide–binding homology domains regulate deactivation gating in hERG channels. *J. Gen. Physiol.* 142:351–366. https://doi.org/10.1085/jgp.201310995

Goodchild, S.J., L.C. Macdonald, and D. Fedida. 2015. Sequence of gating charge movement and pore gating in HERG activation and deactivation pathways. *Biophys. J.* 108:1435–1447. https://doi.org/10.1016/j.bpj.2015.02.014

Gustina, A.S., and M.C. Trudeau. 2009. A recombinant N-terminal domain fully restores deactivation gating in N-truncated and long QT syndrome mutant hERG potassium channels. *Proc. Natl. Acad. Sci. USA.* 106:13082–13087. https://doi.org/10.1073/pnas.0900180106

Guy, H.R., S.R. Durell, J. Warmke, R. Drysdale, and B. Ganetzky. 1991. Similarities in amino acid sequences of Drosophila eag and cyclic nucleotide-gated channels. *Science.* 254:730. https://doi.org/10.1126/science.1658932

Haitin, Y., A.E. Carlson, and W.N. Zagotta. 2013. The structural mechanism of KCNH-channel regulation by the eag domain. *Nature.* 501:444–448. https://doi.org/10.1038/nature12487

Hille, B. 2001. Ion Channels of Excitable Membranes. Oxford University Press, New York. 814 pp.

Kalstrup, T., and R. Blunck. 2013. Dynamics of internal pore opening in $K_{(V)}$ channels probed by a fluorescent unnatural amino acid. *Proc. Natl. Acad. Sci. USA.* 110:8272–8277. https://doi.org/10.1073/pnas.1220398110

Kwan, D.C., D.L. Prole, and G. Yellen. 2012. Structural changes during HCN channel gating defined by high affinity metal bridges. *J. Gen. Physiol.* 140:279–291. https://doi.org/10.1085/jgp.201210838

Lee, C.H., and R. MacKinnon. 2017. Structures of the Human HCN1 Hyperpolarization-Activated Channel. *Cell.* 168:111–120.e11. https://doi.org/10.1016/j.cell.2016.12.023

Li, M., X. Zhou, S. Wang, I. Michailidis, Y. Gong, D. Su, H. Li, X. Li, and J. Yang. 2017. Structure of a eukaryotic cyclic-nucleotide-gated channel. *Nature.* 542:60–65. https://doi.org/10.1038/nature20819

Li, X., A. Anishkin, H. Liu, D.B. van Rossum, S.V. Chintapalli, J.K. Sassic, D. Gallegos, K. Pivaroff-Ward, and T. Jegla. 2015. Bimodal regulation of an Elk subfamily K^+ channel by phosphatidylinositol 4,5-bisphosphate. *J. Gen. Physiol.* 146:357–374. https://doi.org/10.1085/jgp.201511491

Männikkö, R., S. Pandey, H.P. Larsson, and F. Elinder. 2005. Hysteresis in the voltage dependence of HCN channels: Conversion between two modes affects pacemaker properties. *J. Gen. Physiol.* 125:305–326. https://doi.org/10.1085/jgp.200409130

Mannuzzu, L.M., M.M. Moronne, and E.Y. Isacoff. 1996. Direct physical measure of conformational rearrangement underlying potassium channel gating. *Science.* 271:213–216. https://doi.org/10.1126/science.271.5246.213

Marques-Carvalho, M.J., N. Sahoo, F.W. Muskett, R.S. Vieira-Pires, G. Gabant, M. Cadene, R. Schönherr, and J.H. Morais-Cabral. 2012. Structural, biochemical, and functional characterization of the cyclic nucleotide binding homology domain from the mouse EAG1 potassium channel. *J. Mol. Biol.* 423:34–46. https://doi.org/10.1016/j.jmb.2012.06.025

Morais Cabral, J.H., A. Lee, S.L. Cohen, B.T. Chait, M. Li, and R. Mackinnon. 1998. Crystal structure and functional analysis of the HERG potassium channel N terminus: a eukaryotic PAS domain. *Cell.* 95:649–655. https://doi.org/10.1016/S0092-8674(00)81635-9

Muskett, F.W., S. Thouta, S.J. Thomson, A. Bowen, P.J. Stansfeld, and J.S. Mitcheson. 2011. Mechanistic insight into human ether-à-go-go-related gene (hERG) K^+ channel deactivation gating from the solution structure of the EAG domain. *J. Biol. Chem.* 286:6184–6191. https://doi.org/10.1074/jbc.M110.199364

Ng, C.A., M.J. Hunter, M.D. Perry, M. Mobli, Y. Ke, P.W. Kuchel, G.F. King, D. Stock, and J.I. Vandenberg. 2011. The N-terminal tail of hERG contains an amphipathic α-helix that regulates channel deactivation. *PLoS One.* 6:e16191. https://doi.org/10.1371/journal.pone.0016191

Ng, C.A., Y. Ke, M.D. Perry, P.S. Tan, A.P. Hill, and J.I. Vandenberg. 2013. C-terminal β9-strand of the cyclic nucleotide-binding homology domain stabilizes activated states of Kv11.1 channels. *PLoS One.* 8:e77032. https://doi.org/10.1371/journal.pone.0077032

Pardo, L.A., and W. Stühmer. 2014. The roles of $K(^+)$ channels in cancer. *Nat. Rev. Cancer.* 14:39–48. https://doi.org/10.1038/nrc3635

Prole, D.L., and G. Yellen. 2006. Reversal of HCN channel voltage dependence via bridging of the S4–S5 linker and Post-S6. *J. Gen. Physiol.* 128:273–282. https://doi.org/10.1085/jgp.200609590

Robertson, G.A., J.M. Warmke, and B. Ganetzky. 1996. Potassium currents expressed from Drosophila and mouse eag cDNAs in Xenopus oocytes. *Neuropharmacology.* 35:841–850. https://doi.org/10.1016/0028-3908(96)00113-X

Rossi, A.M., and C.W. Taylor. 2011. Analysis of protein-ligand interactions by fluorescence polarization. *Nat. Protoc.* 6:365–387. https://doi.org/10.1038/nprot.2011.305

Sakata, S., Y. Jinno, A. Kawanabe, and Y. Okamura. 2016. Voltage-dependent motion of the catalytic region of voltage-sensing phosphatase monitored by a fluorescent amino acid. *Proc. Natl. Acad. Sci. USA.* 113:7521–7526. https://doi.org/10.1073/pnas.1604218113

Splawski, I., J. Shen, K.W. Timothy, M.H. Lehmann, S. Priori, J.L. Robinson, A.J. Moss, P.J. Schwartz, J.A. Towbin, G.M. Vincent, and M.T. Keating. 2000. Spectrum of mutations in long-QT syndrome genes. KVLQT1, HERG, SCN5A, KCNE1, and KCNE2. *Circulation.* 102:1178–1185. https://doi.org/10.1161/01.CIR.102.10.1178

Tan, P.S., M.D. Perry, C.A. Ng, J.I. Vandenberg, and A.P. Hill. 2012. Voltage-sensing domain mode shift is coupled to the activation gate by the N-terminal tail of hERG channels. *J. Gen. Physiol.* 140:293–306. https://doi.org/10.1085/jgp.201110761

Taraska, J.W., M.C. Puljung, N.B. Olivier, G.E. Flynn, and W.N. Zagotta. 2009. Mapping the structure and conformational movements of proteins with transition metal ion FRET. *Nat. Methods.* 6:532–537. https://doi.org/10.1038/nmeth.1341

Terlau, H., S.H. Heinemann, W. Stühmer, O. Pongs, and J. Ludwig. 1997. Amino terminal-dependent gating of the potassium channel rat eag is compensated by a mutation in the S4 segment. *J. Physiol.* 502:537–543. https://doi.org/10.1111/j.1469-7793.1997.537bj.x

Trudeau, M.C., J.W. Warmke, B. Ganetzky, and G.A. Robertson. 1995. HERG, a human inward rectifier in the voltage-gated potassium channel family. *Science.* 269:92–95. https://doi.org/10.1126/science.7604285

Trudeau, M.C., S.A. Titus, J.L. Branchaw, B. Ganetzky, and G.A. Robertson. 1999. Functional analysis of a mouse brain Elk-type K^+ channel. *J. Neurosci.* 19:2906–2918.

Varnum, M.D., K.D. Black, and W.N. Zagotta. 1995. Molecular mechanism for ligand discrimination of cyclic nucleotide-gated channels. *Neuron.* 15:619–625. https://doi.org/10.1016/0896-6273(95)90150-7

Wang, W., and R. MacKinnon. 2017. Cryo-EM Structure of the Open Human Ether-à-go-go-Related K^+ Channel hERG. *Cell.* 169:422–430.e10. https://doi.org/10.1016/j.cell.2017.03.048

Wang, J., C.D. Myers, and G.A. Robertson. 2000. Dynamic control of deactivation gating by a soluble amino-terminal domain in HERG K^+ channels. *J. Gen. Physiol.* 115:749–758. https://doi.org/10.1085/jgp.115.6.749

Warmke, J.W., and B. Ganetzky. 1994. A family of potassium channel genes related to eag in Drosophila and mammals. *Proc. Natl. Acad. Sci. USA.* 91:3438–3442. https://doi.org/10.1073/pnas.91.8.3438

Warmke, J., R. Drysdale, and B. Ganetzky. 1991. A distinct potassium channel polypeptide encoded by the Drosophila eag locus. *Science.* 252:1560–1562. https://doi.org/10.1126/science.1840699

Whicher, J.R., and R. MacKinnon. 2016. Structure of the voltage-gated K^+ channel Eag1 reveals an alternative voltage sensing mechanism. *Science.* 353:664–669. https://doi.org/10.1126/science.aaf8070

Zagotta, W.N., M.T. Gordon, E.N. Senning, M.A. Munari, and S.E. Gordon. 2016. Measuring distances between TRPV1 and the plasma membrane using a noncanonical amino acid and transition metal ion FRET. *J. Gen. Physiol.* 147:201–216. https://doi.org/10.1085/jgp.201511531

Zhang, X., F. Bertaso, J.W. Yoo, K. Baumgärtel, S.M. Clancy, V. Lee, C. Cienfuegos, C. Wilmot, J. Avis, T. Hunyh, et al. 2010. Deletion of the potassium channel Kv12.2 causes hippocampal hyperexcitability and epilepsy. *Nat. Neurosci.* 13:1056–1058. https://doi.org/10.1038/nn.2610

Zhao, Y., M.P. Goldschen-Ohm, J.H. Morais-Cabral, B. Chanda, and G.A. Robertson. 2017. The intrinsically liganded cyclic nucleotide–binding homology domain promotes KCNH channel activation. *J. Gen. Physiol.* 149:249–260. https://doi.org/10.1085/jgp.201611701

Zheng, J., and W.N. Zagotta. 2003. Patch-clamp fluorometry recording of conformational rearrangements of ion channels. *Sci. STKE.* 2003:PL7.